American Society of Mechanical Engineers

ASME Pre-Print Repository

Institutional Repository Cover Sheet

Ecole Polytechnique Fédérale de Lausanne, Switzerland
Infoscience (https://infoscience.epfl.ch/)
https://infoscience.epfl.ch/record/277568

Elia	Iseli	elia.iseli@fischerspindle.com
First	*Last*	*E-mail*

Analysis of spiral-grooved gas journal bearings by the narrow-groove theory and the finite element method at large eccentricities

Elia Iseli*
Fischer Spindle AG
Ernst Fischer-Weg 5
CH-3360 Herzogenbuchsee, Switzerland
Email: elia.iseli@fischerspindle.com

Eliott Guenat
Ecole Polytechnique Fédérale Lausanne
EPFL STI IGM LAMD
Maladière 71b, CP526
CH-2002 Neuchâtel 2, Switzerland
Email: eliott.guenat@epfl.ch

Roger Tresch
Fischer Spindle AG
Ernst Fischer-Weg 5
CH-3360 Herzogenbuchsee, Switzerland
Email: roger.tresch@fischerspindle.com

Jürg Schiffmann
Professor
Ecole Polytechnique Fédérale Lausanne
EPFL STI IGM LAMD
Maladière 71b, CP526
CH-2002 Neuchâtel 2, Switzerland
Email: jurg.schiffmann@epfl.ch

ABSTRACT

A finite groove approach (FGA), based on the finite element method (FEM), is used for analyzing the static and dynamic behavior of spiral-grooved aerodynamic journal bearings at different eccentricities, number of grooves and compressibility numbers. The results of the FGA are compared with the narrow-groove theory (NGT) solutions. For the rotating-groove case a novel time-periodic solution method is presented for computing the quasi-steady state and dynamic pressure profiles. The new method offers the advantage of avoiding time-consuming transient integration, while resolving a finite number of grooves. The static and dynamic solutions of the NGT and FGA approach are compared and they show good agreement, even at large eccentricities ($\varepsilon = 0.8$) and high compressibility numbers

---
*Corresponding author

($\Lambda = 70$). Stability maps at different eccentricities are presented. At certain operation points, a stability decrease towards larger eccentricities is observed. The largest stability deviations of the NGT from the FGA solutions occur at large groove angle, low number of grooves and large compressibility numbers.

1 Introduction

In a broad field of energy conversion applications, high-speed small-scale turbomachinery is used to increase the overall efficiencies of systems such as domestic or commercial scale heat pumps [22], Organic Rankine cycles [19] or fuel cells [26] to name a few.. Most of these applications require a high degree of working fluid purity, ruling out oil lubricated rotating systems. Therefore, gas lubricated bearings are used, such as herringbone groove journal bearings (HGJB). Beside oil-free operation, HGJBs provide additional advantages, such as long lifetime, high rotational speed with relatively low frictional losses, no sealing requirements and avoidance of auxiliary systems. However, in order to correctly predict the rotordynamic system performance, accurate HGJB models are required.

Nature of the issue. The analysis of grooved aerodynamic bearings was firstly introduced by Whipple [25], who investigated grooved thrust bearings by applying the narrow-groove theory (NGT), assuming local incompressibility across a groove-ridge pair and an infinite number of grooves. The NGT was then used for computing the static and dynamic behavior of HGJBs by Hirs [13], Malanoski and Pan [16], Vohr and Pan [23] and Vohr and Chow [24]. By means of a perturbation analysis, they obtained the linearized dynamic bearing properties, allowing for the computation of the bearing stability. With this method Fleming and Hamrock [10, 6] optimized herringbone grooved journal bearings for maximum load capacity and stability. The analysis was performed for a shaft at concentric position, obtaining a solution valid only at small radial displacements. Castelli and Vohr [3] extended the analysis to larger eccentricities and presented performance charts, showing the influence of bearing geometry, eccentricity, compressibility number and misalignment on the load capacity, the attitude angle and the restoring moment. The obtained results were compared with the experimental data of Malanoski [15]. Their analysis suggests that the numerical results overpredict the radial load capacity, which has been partially attributed to the edge effect. The edge effect has been discussed in more detail by Muijderman [18] for thrust bearings, operated with an incompressible lubrication fluid.

The influence of groove number on gas-lubricated bearing performance has often been neglected and only a few papers have addressed this topic. The analysis of gas bearings with a small number of grooves has been investigated by Bonneau and Absi [2]. They applied an upwind finite element method (FEM), using non-symmetrical weight functions proposed by Heinrich [12] and presented radial load capacity, stiffness and damping values for bearings with rotating and non-rotating grooves. The pressure field for rotating grooves was computed by means of a transient analysis. The results were compared with NGT solutions and large discrepancies were reported. However, the NGT was only used at concentric shaft positions and compared with FEM solutions at eccentric positions.

Goals and objectives. The goal of the investigation is a thorough comparison between the classical NGT and a more advanced FEM based solver and to identify the prediction limitations of the two methodologies.The objectives are to: (1)

implement solver methods for computing the HGJB reaction forces by means of a perturbation analysis at eccentric positions for different number of rotating and non-rotating grooves, (2) investigate the influence of shaft eccentricity on bearing stability, (3) identify the limitations of the NGT at concentric and eccentric shaft position.

Scope of the paper. The perturbation analysis is applied to the compressible Reynolds equation. The NGT equation is solved by a finite difference scheme and the FGA by means of a FEM. A novel time-periodic computation method is presented, for computing bearings with a finite number of rotating grooves. The computation methods are compared at different bearing operational conditions. The steady-state/quasi steady-state and the dynamic bearing behavior are investigated and the influence of shaft eccentricity and number of grooves on bearing performance are discussed for compressibilities up to 40 and for different geometries.

2   Theory

The fluid film of an aerodynamic bearing can be described by the compressible Reynolds equation, which is derived from the Navier-Stokes-equations by assuming a Newtonian, isoviscous fluid with negligible inertia effect, operating as a thin film (properties across the film thickness are constant) [11]. Under the assumption of an ideal gas, the density can be replaced by the pressure for a given temperature and the Reynolds equation in vector notation can be written as:

$$\Lambda \frac{\partial PH}{\partial \tau} = \nabla \cdot \left(H^3 P \boldsymbol{\nabla} P \right) - \Lambda \boldsymbol{\nabla} \left(PH \right) \cdot \boldsymbol{q}_\theta \tag{1}$$

where $\vec{q}_\theta$ is a unit vector parallel to the velocity vector of the moving surface, τ the non-dimensional time, H the non-dimensional fluid film height, P the non-dimensional fluid pressure and Λ the compressibility number.

In the derivation of the Reynolds equation no restriction to the surface topology is made and Eq. (1) can directly be applied to grooved surfaces. For HGJBs, the local clearance takes different values, depending on whether the observation point is located at a groove or at a ridge. If the groove depth is non zero a triangular shaped pressure profile is obtained, which is stationary for stationary grooves and time-dependent, for rotating grooves. Therefore, grooves attached to the rotating surface and grooves attached to the stationary surface have to be treated differently.

Bearing specification. A classical herringbone grooved journal bearing can be specified by its diameter, length to diameter ratio, groove angle, groove width ratio, groove length ratio, film thickness ratio and number of grooves. The parameters are listed in Table 1 and schematically shown in Fig. 1. For traditional bearings α, β and H_{gr} are constant along the axial direction Z. However, they can also be specified as functions of Z, as it has been presented by Schiffmann [21], thus offering a larger set of optimization parameters, hence more advanced designs are possible. In this work, only traditional bearings are investigated with constant bearing parameters along the axial direction.

For the static analysis, the bearing introduced by Vohr and Chow [24] is used. The bearing geometry is specified by $L/D = 1$, $H_{gr} = 2.1$, $\alpha = 0.5$, $\beta = 32.8°$, $\gamma = 1$.

In the lower schematic of Fig. 1, the groove geometry is visualized. Depending on whether the grooves are on the

rotating or on the stationary surface, the upper geometry represents the rotor or the bushing respectively, and vice versa the lower geometry.

Narrow Groove Theory. If an infinite number of grooves is assumed, Eq. (1) can be simplified, yielding the NGT equation. Since the number of grooves approaches infinity, a smooth pressure profile solution is obtained, both for the rotating and the non-rotating groove configuration. By assuming an infinite number of grooves and local incompressibility, the NGT equation can be derived in analogy to Vohr and Chow [24]. Using the same nomenclature as Guenat et al. [7] it follows:

$$
\begin{aligned}
\frac{\partial}{\partial \theta} & \left(P \left[f_1 \frac{\partial P}{\partial \theta} + f_2 \frac{\partial P}{\partial Z} + c_s f_4 \sin \beta \right] \right) + \\
\frac{\partial}{\partial Z} & \left(P \left[f_2 \frac{\partial P}{\partial \theta} + f_3 \frac{\partial P}{\partial Z} - c_s f_4 \cos \beta \right] \right) = \\
& \sigma \frac{\partial (P f_5)}{\partial \tau} + \Lambda \frac{\partial (P f_5)}{\partial \theta},
\end{aligned}
\tag{2}
$$

where θ is the circumferential coordinate, Z the axial coordinate, P the non-dimensional fluid pressure, β the spiral-groove angle, τ the non-dimensional time, σ the squeeze number and Λ the compressibility number. The coefficients f_i and c_s are non-dimensional parameters, specified by the bearing geometry and operational condition. Their formulas are given by Guenat [7]. Eq. (2) represents a two dimensional non-linear transient partial differential equation (PDE).

In case of a perturbation analysis, the equation is linearized by introducing a perturbed clearance and a perturbed pressure. The perturbed clearance can be written as follows:

$$
H_{per} = H + \Delta x H_x(\theta) e^{i\omega_{ext}} + \Delta y H_y(\theta) e^{i\omega_{ext}},
\tag{3}
$$

with

$$
H = H_{0r,g} + \varepsilon_x \cos(\theta) + \varepsilon_y \sin(\theta),
\tag{4}
$$

where $H_{0r,g}$ is the non-dimensional ridge and groove gap height respectively, $\varepsilon_x, \varepsilon_y$ the static shaft eccentricities, $H_x = \cos\theta$, $H_y = \sin\theta$ the perturbed gap height variations in circumferential direction and $\Delta x, \Delta y \ll 1$ are the amplitudes of the perturbations. The perturbed pressure is given as follows:

$$
P_{per} = P + \Delta x P_x(\theta, z) e^{i\omega_{ext}} + \Delta y P_y(\theta, z) e^{i\omega_{ext}}
\tag{5}
$$

Inserting these expressions into Eq. (2) and into the NGT coefficients f_i, c_s and collecting all zeroth and first order terms ($O(\Delta x), O(\Delta y)$), one zeroth and two first order equations (x and y direction) are obtained. Each of them is solved individually in order to obtain the static and dynamic pressure fields. The static bearing reaction forces are computed by integrating the zeroth order pressure field:

$$f_x = -p_a R^2 \int_{-L/D}^{L/D} \int_0^{2\pi} (P-1) \cos\theta \, d\theta \, dZ \tag{6}$$

$$f_y = -p_a R^2 \int_{-L/D}^{L/D} \int_0^{2\pi} (P-1) \sin\theta \, d\theta \, dZ. \tag{7}$$

The radial force coefficient and attitude angle for a shaft displaced in x-direction can be computed by:

$$F_r = \frac{f_x}{\varepsilon_x p_a L D}. \tag{8}$$

and:

$$\phi = \arctan\left(\frac{f_y}{f_x}\right). \tag{9}$$

The dynamic coefficients are obtained by integrating the first order pressure fields P_x and P_y. This yields impedance values, from which the stiffness and the damping coefficients are extracted by using the following relation:

$$\begin{bmatrix} Z_{xx} & Z_{xy} \\ Z_{yx} & Z_{yy} \end{bmatrix} = \begin{bmatrix} K_{xx} & K_{xy} \\ K_{yx} & K_{yy} \end{bmatrix} + i\omega_{ex} \begin{bmatrix} C_{xx} & C_{xy} \\ C_{yx} & C_{yy} \end{bmatrix}. \tag{10}$$

Lund's [14] method is used for assessing the bearing stability. A critical mass is introduced, which specifies the maximum mass the bearing can support before it gets unstable. The critical mass is obtained by finding the critical excitation frequency

$\omega_{ex,c}$ at which the imaginary part of the equivalent impedance Z of the point-mass-bearing system is zero:

$$Im(Z(\omega_{ex,c})) = 0, \tag{11}$$

where Z is obtained with [8]:

$$Z = \frac{1}{2}(Z_{xx} + Z_{yy}) \pm \sqrt{\frac{1}{4}(Z_{xx} - Z_{yy})^2 + Z_{xy}Z_{yx}}. \tag{12}$$

The critical mass is computed by the following relation:

$$m_{crit} = \frac{Z(\omega_{ex,c})}{\omega_{ex,c}^2}. \tag{13}$$

The corresponding non-dimensional critical mass is defined as follows [6]:

$$M_{crit} = m_{crit} \frac{p_a}{2\mu^2 L} \left(\frac{h_{0r}}{R}\right)^5. \tag{14}$$

FGA: non-rotating grooves. For the case where the grooves are attached to the non-rotating surface, the Reynolds equation (Eq. (1)) can be linearized in the same way as for the NGT equation. The zeroth order equation is written as follows:

$$\nabla \cdot \left(H^3 P \nabla P\right) - \Lambda \nabla (PH) \cdot \boldsymbol{q}_\theta = 0 \tag{15}$$

The first order equation in x-direction follows with:

$$\nabla \cdot \left(PH^3 \nabla P_x + \left(P_x H^3 + 3PH^2 H_x\right) \nabla P\right) =$$
$$\Lambda \left(\nabla (PH_x) + \nabla (P_x H)\right) \cdot \boldsymbol{q}_\theta + \tag{16}$$
$$i\sigma \left(P_x H + PH_x\right).$$

Both equations can be written in weak form by applying the Petrov-Galerkin method. Eq. (15) and Eq. (16) are multiplied by

the weight function W and integrated over an element. Applying partial integration the weak form is obtained for the zeroth order equation:

$$\int\limits_{\Omega_e} \left(PH^3 \nabla W \cdot \nabla P - \Lambda PH \nabla W \cdot \boldsymbol{q}_\theta \right) d\Omega_e =$$

$$\int\limits_{\partial\Omega_e} W \left(PH^3 \nabla P - \Lambda PH \boldsymbol{q}_\theta \right) \cdot \boldsymbol{n} d\Gamma \tag{17}$$

and for the first order equation:

$$\int\limits_{\Omega_e} \big\{ PH^3 \nabla P_x \cdot \nabla W + \left(P_x H^3 + 3PH^2 H_x \right) \nabla P \cdot \nabla W -$$

$$\left(PH_x + P_x H \right) \left(\Lambda \nabla W \cdot \boldsymbol{q}_\theta - iW\sigma \right) \big\} d\Omega_e =$$

$$\int\limits_{\partial\Omega_e} W \big\{ PH^3 \nabla P_x + \left(P_x H^3 + 3PH^2 H_x \right) \nabla P -$$

$$\Lambda \left(PH_x + P_x H \right) \boldsymbol{q}_\theta \big\} \cdot \boldsymbol{n} d\Gamma. \tag{18}$$

The boundary integral terms are omitted, based on the reasonings by Miller and Green [17].

At the bearing edges Dirichlet boundary conditions are imposed:

$$P = 1, P_x = P_y = 0 \quad \text{on } \partial\Gamma.$$

At the symmetry line of the bearing (for only radially displaced bearings) the natural boundary condition is imposed for the static and the dynamic pressure fields:

$$\frac{\partial P}{\partial Z} = \frac{\partial P_{x,y}}{\partial Z} = 0 \quad \text{at Z=0.}$$

For the whole solution domain the periodic boundary condition is applied:

$$P(\theta, Z) = P(\theta + 2\pi, Z),$$

$$P_{x,y}(\theta, Z) = P_{x,y}(\theta + 2\pi, Z).$$

The static and dynamic forces are computed as presented above with Eqs. (6), (7) and (10).

FGA: rotating grooves In the case of rotating grooves, no steady-state solution exist. Bonneau and Absi [1] solved Eq. (1) transiently by integrating in time until quasi-steady state was reached. This procedure leads however, to very time-consuming computations. A new methodology is presented here, the time-periodic approach, which allows the computation of the quasi-steady state pressure profile directly, without time integration, thus decreasing the computational time by two orders of magnitude compared to the approach by Bonneau and Absi [1]. The comparison of CPU time of the different solvers for rotating grooves are presented in Table 3.

The bearing in eccentric position $(\varepsilon_x, \varepsilon_y)$ is schematically shown in Fig. 2. The grooved shaft with radius R is rotating with rotational speed Ω in counter-direction to the circumferential direction θ. In this time-periodic approach the mesh is attached to the rotating grooves and the pressure field is computed in the rotating coordinate system x', y'. The angle between the stationary and rotating coordinate systems is 2τ. The concentric film clearance is h_{0r} at the ridges and h_{0g} at the grooves.

As in the case of non-rotating grooves, Eq. (1) is linearized around the static eccentricity, however, all pressure and local film thickness terms in the reference frame (x, y) are time dependent and the zeroth and the first order equations remain transient equations. For a grooved shaft that rotates in the negative θ direction, the film gap height is defined as:

$$H(\theta, \tau) = H_{0r,g} + \varepsilon_x \cos(\theta - 2\tau) + \varepsilon_y \sin(\theta - 2\tau). \tag{19}$$

where $H_{0r,g}$ is the local fluid film thickness expressed in the coordinate frame attached to the grooved rotating member. The zeroth order equation can be written as:

$$\nabla \cdot (H^3 P \nabla P) - \Lambda \nabla (PH) \cdot \boldsymbol{q}_\theta = \Lambda \left(P \frac{\partial H}{\partial \tau} + H \frac{\partial P}{\partial \tau} \right) \tag{20}$$

and the first order equation follows with:

$$\nabla \cdot \left(H^3 \nabla (PP_x) + 3PH^2 H_x \nabla P \right) =$$
$$\Lambda \left(\nabla (PH_x + P_x H) \cdot \boldsymbol{q}_\theta + \right.$$
$$\left. \frac{\partial (HP_x)}{\partial \tau} + \frac{\partial (H_x P)}{\partial \tau} \right) +$$
$$i\sigma (P_x H + PH_x). \tag{21}$$

Author: Elia Iseli, Page 8

Eq. (20) has the same form as Eq. (1), except for the film clearance, that varies periodically in time τ and circumferential direction θ due to the rotating grooves. The periodic arrangement of groove-ridge pairs and the constant rotor speed lead to the following implications on the quasi-steady state pressure profile:

the pressure is periodic at any given time: $P(\theta, Z, \tau) = P(\theta + 2\pi, Z, \tau)$

the pressure value at point $(\theta + 2\pi/N_g, Z)$ and time τ is equal to the pressure value at point (θ, Z) and time $\tau + \pi/N_g$.

where N_g is the number of grooves. This space-time dependency can be expressed mathematically as follows:

$$P(\theta, Z, \tau + \pi n/N_g) = P(\theta + 2\pi n/N_g, Z, \tau) \tag{22}$$

with $n = 0, 1, 2, \ldots$.

This means, that the pressure at a given angular location within a groove-ridge pair of a rotor at a constant static eccentricity follows a periodic function p_t in time, which can be related to space by $\theta_0 - 2\tau$, where θ_0 represents the circumferential position at time $\tau = 0$. Since the grooves are geometrically identical, the periodic function will go through N_g points. This is schematically shown in Fig. 3.

The periodic function $p_t(\theta)$ can be used to link time with space:

$$\frac{\partial P}{\partial \tau} = 2 \frac{\partial p_t(\theta)}{\partial \theta}. \tag{23}$$

In order to solve Eq. (20), an analytical expression for p_t as a function of pressure values P_i in the reference frame has to be found. This is done by applying the discrete Fourier transformation (DFT) to the groove-ridge periodic points:

$$p_t(\theta) = \frac{1}{N_g} \sum_{k=0}^{N_g-1} c_k e^{ik\theta} \tag{24}$$

with the Fourier coefficient:

$$c_k = \sum_{n=0}^{N_g-1} P_n e^{-i\frac{2\pi}{N_g}nk}, \tag{25}$$

where P_n are the pressure values in the rotating reference frame. Inserting Eqs. (24) and (25) into Eq. (23) yields an expression

for the pressure time derivative in Eq. (20) only as a function of pressure values P_n and circumferential coordinate θ:

$$\frac{\partial P}{\partial \tau} = 2\frac{\partial p_t(\theta)}{\partial \theta} = \frac{1}{N_g}\sum_{k=0}^{N_g-1} 2ik \left(\sum_{n=0}^{N_g-1} P_n e^{-i\frac{2\pi}{N_g}nk}\right) e^{ik\theta} \tag{26}$$

Hence this approach, which exploits the periodic time-space dependency of the pressure evolution and its expression in the rotating frame through a Fourier transformation, allows to get rid of the time dependency.

Eq. (20) together with Eq. (26) represent a complete set of equations for computing directly the quasi-steady state pressure field of a bearing with rotating grooves. The weak form of Eq. (20) is obtained in the same way as for the non-rotating groove case. Based on the same reasonings as for the non-rotating groove case, the boundary integral terms, coming from the partial integration of the weak form, are omitted. The zeroth order and the first order equations are given as follows:

$$\int_{\Omega_e} \left(PH^3\boldsymbol{\nabla}W \cdot \boldsymbol{\nabla}P - \Lambda PH\boldsymbol{\nabla}W \cdot \boldsymbol{q}_\theta + \right.$$
$$\left. \Lambda\frac{\partial(PH)}{\partial \tau} \right) d\Omega_e = 0 \tag{27}$$

$$\int_{\Omega_e} \left\{ PH^3\boldsymbol{\nabla}P_x \cdot \boldsymbol{\nabla}W + \left(P_xH^3 + 3PH^2H_x\right)\boldsymbol{\nabla}P \cdot \boldsymbol{\nabla}W - \right.$$
$$(PH_x + P_xH)\left(\Lambda\boldsymbol{\nabla}W \cdot \boldsymbol{q}_\theta - iW\sigma\right) +$$
$$\left. \Lambda\left(\frac{\partial(HP_x)}{\partial \tau} + \frac{\partial(H_xP)}{\partial \tau}\right) \right\} d\Omega_e = 0. \tag{28}$$

The non-linearity of Eq. (27) is treated by the Newton-Raphson method, which necessitates the computation of the Jacobian. The contribution of the time derivative term $\partial P/\partial \tau$ to the Jacobian can be computed by:

$$\frac{\partial}{\partial P_n}\left(\frac{\partial P}{\partial \tau}\right) = \frac{1}{N_g}\sum_{k=0}^{N_g-1} 2ik \left(e^{-i\frac{2\pi}{N_g}nk}\right) e^{ik\theta}. \tag{29}$$

Since the Jacobian of the time derivative term is independent on the pressure values P_n, it has to be computed only once for the complete iteration procedure, which represents a significant time gain.

After solving Eqs. (27) and (28), the static reaction forces, expressed in the static frame of reference, attached to the

bushing, are computed by:

$$f_x(\tau) = -p_a R^2 \int\limits_{-L/D}^{L/D} \int\limits_0^{2\pi} (P-1)\cos(\theta - 2\tau) \, d\theta dZ \tag{30}$$

$$f_y(\tau) = -p_a R^2 \int\limits_{-L/D}^{L/D} \int\limits_0^{2\pi} (P-1)\sin(\theta - 2\tau) \, d\theta dZ. \tag{31}$$

In analogy, the bearing impedances are computed and the dynamic forces follow with Eq. (10). The static and the dynamic forces are functions of τ, however, at quasi-steady state, despite the rotating pressure field, the fluctuation of f_x and f_y has been found to be negligible. The ratio of fluctuation amplitude to mean force value is below $0.2\,\%$ for a bearing with 8 grooves ($\varepsilon < 0.8$, $\Lambda < 40$ and varying L/D) and is mainly numerically related. Increasing the number of grooves, reduces the periodic reaction force fluctuation. Therefore, all results in this paper have been obtained at $\tau = 0$.

3 Results and discussion

Grid sensitivity study and code verification The FEM integration was performed by Gauss quadrature and the non-linearities were treated by the Newton-Raphson method. Throughout all computations, the iteration tolerance was set to 1×10^{-5}. The convergence criteria was defined as:

$$\|P^{(n+1)} - P^{(n)}\| < 1 \times 10^{-5}, \tag{32}$$

where P represents the solution vector and (n) the iteration step.

The different solvers are checked by means of a grid sensitivity study. The study was conducted at $\Lambda = 70$ and an eccentricity of $\varepsilon = 0.8$, which was found to be the worst operation point in terms of convergence for the range of interest. The sensitivity analysis was performed for rotating and non-rotating grooves for the 2D-NGT and the FEM solver. The results and the used mesh sizes are presented in the appendix.

The FEM code was verified by the method of manufactured solutions, accordingly to Salari et al. [20]. An error convergence study was performed and an order of accuracy of 2 could be confirmed.

3.1 Comparison of steady state solution

Grooved bearing, non-rotating grooves. In analogy to Bonneau and Absi [1] the radial force coefficient and the attitude angle are computed at eccentric positions for bearings with different number of non-rotating grooves. The number of grooves N_g approach infinity for the NGT method and is varied for the FEM analysis between 16 and 30. The domain was meshed by quadrilateral elements and bi-linear shape and weight functions were used.

In Figs. 4 and 5 the results of the FEM analysis and the NGT are presented.

The comparison between the two models suggests that the NGT predicts larger radial force coefficient than the FGA, however the curves follow very closely. The difference increases both with compressibility and eccentricity. Up to $\Lambda = 40$ the difference between models is $< 3.0\%$. It can also be seen, that the bearing with 30 grooves has a smaller deviation from the NGT solution, compared to the bearing with 16 grooves, which corroborates the hypothesis of the NGT (infinite number of grooves).

The attitude angle of the FGA and the NGT solution show good agreement. It is remarkable that the NGT and the FEM show better agreement towards high eccentricities. At an eccentricity of $\varepsilon = 0.8$, the curves can hardly be distinguished.

Grooved bearing, rotating grooves. The radial force coefficient and the attitude angle of the same bearing, but with the grooves on the rotating surface, is shown in Figs. 6 and 7. In contrast to the stationary groove case, the radial force coefficients are hardly influenced by the eccentricity, which suggests a high degree of linearity between the force coefficient and eccentricity. In order to be able to distinguish the single curves, only eccentricities of 0.001 and 0.8 are shown. Compared to the FGA the NGT predicts higher F_r for low eccentricities and vice-versa at higher eccentricities. The bearing with 30 grooves shows a better agreement with the NGT, compared to the bearing with 16 grooves. The largest difference of F_r between the NGT and the FGA of the bearing with 30 grooves is below 6 % at $\varepsilon = 0.001$ and $\Lambda = 40$. At larger eccentricities the difference between the NGT and the FEM solution decreases.

A similar trend can be observed for the attitude angle. The largest difference can be found towards larger compressibility numbers. Overall, the comparison between the NGT and the FGA suggests that both approaches yield very similar results with relative deviations well below 6 %.

3.2 Comparison of dynamic first-order perturbed solution

Grooved bearing, non-rotating grooves. Stability operation maps of the NGT and the FGA for a herringbone journal bearing with stationary grooves, are compared at different eccentricities in Figs. 8a to 8d. The minimum critical mass encountered on the compressibility ranging from zero to the one corresponding to the nominal speed is plotted.

The two approaches are in good agreement at low eccentricities and compressibility numbers. The larger the number of grooves, the smaller the difference between the NGT and FGA solution. The constant operation stability zone at larger compressibility numbers ($\Lambda > 10$) disappears towards higher eccentricities, which is predicted by both, the NGT and the FGA. Further, a reduction of number of grooves is suggested to decrease the stability. In Fig. 8c the bearing with $N_g = 8$ shows a reduced stability at $\Lambda > 30$, while bearings with $N_g = 16$ and $N_g = 30$ show the same behavior at higher eccentricity (see Fig. 8d). At an eccentricity of $\varepsilon = 0.8$ and $\Lambda \approx 10 - 20$, the NGT and the bearings with 16 and 30 grooves show increased

stability zones. For bearings with a larger number of grooves, the zone is shifted towards higher compressibility numbers. At compressibility numbers $\Lambda > 20$, the stability region is largest for the bearing with 8 grooves.

Grooved bearing, rotating grooves. For bearings with rotating grooves, the corresponding stability operation maps are shown in Figs. 9a to 9d.

In Fig. 9a the results suggest a region of constant operation stability. This is due to a locally increased bearing stability and therefore increased critical mass. Since the minimum critical mass is plotted, its value is not changed, resulting in a constant curve. Up to eccentricities of $\varepsilon = 0.4$ the constant stability region can be observed for the NGT and the FGA with 16 and 30 grooves. The bearing with 8 grooves losses its constant operation stability region already at $\varepsilon = 0.4$. At larger eccentricities $\varepsilon > 0.6$, the increased stability region disappears for all bearings. The trend is shown by the NGT and the FGA solutions with good agreement. In summary, and from a practical point of view (minimum critical mass), both the NGT and the FGA predict very similar stability maps for compressibility numbers up to 40 and static eccentricities up to 0.4. At larger eccentricities, discrepancies appear, in particular for a low number of grooves.

3.3 Analysis of optimized bearings at different eccentricities

The above considerations are valid for one specific bearing type. In this section, the investigation is extended to a variety of bearing geometries based on Fleming and Hamrock's [6] optimized HGJBs in concentric position for maximum stability.

Figs. 10 to 12 compare the minimum critical masses obtained by both the NGT and the FGA with the ones predicted by Fleming and Hamrock for L/D of 0.5, 1 and 2, operated at different maximum compressibility numbers and static eccentricities. It can be seen, that for all length-to-diameter ratios and compressibility numbers below 10, an increasing static eccentricity has a positive effect on the stability. A concentric bearing stability analysis in this operation range is a conservative approach and therefore justified. For bearings with $L/D = 1$ the stability increase with eccentricity is most significant and even reaches values that are five times the ones obtained at concentric positions.

At compressibility number $\Lambda = 40$ and $L/D = 1$ the stability drastically decreases with increased eccentricity and a bearing design at concentric position my be insufficient for guaranteeing stable operation at all possible shaft positions, unless a safety factor of > 14 is selected. Therefore, the bearing stability analysis has to be extended to eccentricities > 0. For Brg. 3 and Brg. 4 in Fig. 10, Brg. 3 in Fig. 11 the minimum critical mass shows a maximum at an eccentricity between 0 and 0.8, requiring to consider the bearing stability performance both at low and large eccentricities. For bearing 4 in Fig. 11, the stability decrease with eccentricity is most pronounced. Therefore it can be concluded, that depending on the operational condition a bearing stability optimization at concentric position may be insufficient and the bearing performance can be strongly overestimated.

Comparing the 2D-NGT and the FGA solutions, a good agreement can be observed for the bearings with $L/D = 1$ and $L/D = 0.5$ for most eccentricities and compressibility numbers. The bearing with 30 grooves does not always show better agreement with the NGT, which can be explained by the discretized range of compressibility numbers, which does not guarantee to extract exactly the minimum critical mass value.

For a bearing with $L/D = 2$ the difference between 2D-NGT and FGA is large for compressibility numbers $\Lambda > 20$.

This can be attributed to the local compressibility effect, which was investigated in detail by Constantinescu [4].

The optimized bearings at $\Lambda > 20$ (Brg.3 and Brg. 4 in Fig. 12) have a large groove angle $\beta > 50°$, which leads to an increased circumferential groove-ridge width. The increase of number of grooves from 16 to 30, which reduces the groove-ridge width, does still lead to a strong difference, compared to the NGT. In Fig. 13 it can be seen that the groove angle β strongly influences the local pressure profile shape. The combination of a large Λ and β leads to a pressure profile that is completely different to a linear shape, as it would be for local incompressibility (assumption of the NGT). For larger L/D values, the impact on the bearing reaction forces is even bigger, since the pressure profile, which is not linear in its shape, is integrated on a larger fluid domain, resulting in a even bigger discrepancy between NGT and FGA. Therefore, the high L/D value in combination with the large groove angle β can be identified as the causes for the large discrepancies between the NGT and the FGA solutions in Fig. 12, and the NGT field of validity is exceeded.

Typical values of the above mentioned parameters, used for experimental investigations (e.g. Cunningham [5] and Guenat [9]), are compressibility numbers of $\Lambda = 0 - 40$, spiral-groove angles $\beta = 10 - 40°$ and $L/D = 1$. In this region, the local compressibility effects are less severe and the NGT and the FGA show good agreement.

4 Summary and Conclusion

Aerodynamic bearings with grooves on the non-rotating and on the rotating surface were investigated at different compressibility numbers and eccentricities. A novel method for computing the quasi-steady state solution of the compressible Reynolds equation for rotating grooves was introduced, which allows to discretize the grooved surface. The method, resolving the number of grooves, is called the Finite Groove Approach (FGA). The narrow groove theory NGT was applied and compared against FGA based solutions with different number of grooves. The static and dynamic bearing properties were compared in order to investigate the field of applicability of the different solvers. The following can be stated for bearings with groove angles $\beta < 35°$:

1. Compared to the FGA solution with $N_g = 30$, the NGT overestimates the radial force coefficient F_r for stationary grooves, by a maximum of 3.7 % for compressibilities up to $\Lambda = 40$ and eccentricities $\varepsilon < 0.8$. However, the NGT and FGA solution show in a wide range of operation points with a much better agreement, even at high eccentricities and compressibility number.

2. The radial force coefficient of bearings with rotating grooves is hardly influenced by the eccentricity. The NGT and the FGA solutions show the same trend with a maximum difference of 6 % at $\varepsilon = 0.001$ and $\Lambda = 40$. The NGT and the FGA solution show better agreement at larger eccentricities.

3. The minimum critical masses, computed by the NGT and the FGA, show good agreement even at large eccentricities. Bearings with a lower number of non-rotating grooves show a smaller stability region at high eccentricities. Increasing the number of non-rotating grooves leads to an increased region of stability.

4. Depending on the compressibility number, the bearing stability increases or decreases towards larger eccentricities.

A concentric bearing stability analysis may be insufficient, depending on the bearing geometry and the operational conditions and the investigation has to be extended, covering large eccentricities.

It can be concluded that the NGT field of applicability even covers large eccentricities and high compressibility numbers, which allows the usage of the NGT over a wide range of operational conditions.

However, if $\beta > 35°$ and $\Lambda > 20$, the NGT and the FGA with finite number of grooves ($N_g < 30$) show large discrepancies, which are caused by the increased compressibility effect, leading to a pressure profile that strongly deviates from a linear shape, as it is assumed by the NGT. Therefore, it can be stated that the NGT field of applicability is restricted by the number of grooves, the compressibility and the groove angle. The influence of these three parameters has to be carefully considered, before the NGT is applied.

Nomenclature

q	=	Unit vector
C	=	Non-dimensional damping
c	=	Fourier coefficient
c_s	=	NGT coefficient
D	=	Diameter (m)
f	=	Force (N)
f	=	NGT coefficient
F_r	=	Force coefficient
H	=	Non-dimensional gap height
h	=	Gap height µm
i	=	Imaginary number ($\sqrt{-1}$)
K	=	Non-dimensional stiffness
L	=	Bearing length (m)
M_{crit}	=	Dimensionless critical mass, $m p_a (h_{0r}/R)^5/(2L\mu^2)$
m_{crit}	=	Critical mass of shaft (kg)
n	=	Natural number
N_g	=	Number of grooves
P	=	Non-dimensional pressure
p_a	=	Ambient pressure (Pa)
p_t	=	Time periodic function
P_x	=	Dimensionless, dynamic pressure in x-direction
P_y	=	Dimensionless, dynamic pressure in y-direction
R	=	Radius (m)
t	=	Time (s)
W	=	Weight function
w	=	Width (m)
x	=	Coordinate in shaft cross-section plane
y	=	Coordinate in shaft cross-section plane
Z	=	Non-dimensional axial coordinate, $Z = z/R$
Z	=	Non-dimensional impedance
z	=	Axial coordinate (m)
α	=	Dimensionless groove width
β	=	Groove angle (deg)
Γ	=	Boundary
γ	=	Dimensionless groove length
Λ	=	Compressibility number, $6\mu\Omega/p_a(R/h)^2$
Λ_1	=	Compressibility number based on speed of grooved surface, $6\mu\Omega_1/p_a(R/h)^2$
Λ_2	=	Compressibility number based on speed of smooth surface, $6\mu\Omega_2/p_a(R/h)^2$

μ = Dynamic viscosity (Pa·s)
Ω = Rotational speed (rad/s)
Ω_1 = Rotational speed of grooved member (rad/s)
Ω_2 = Rotational speed of smooth member (rad/s)
ω_{ex} = Excitation frequency (rad/s)
ϕ = Attitude angle (deg)
σ = Squeeze number, $12\mu\omega_{ex}/p_a(R/h)^2$
τ = Non-dimensional time, $\Omega t/2$
θ = Circumferential coordinate (rad)
ε = Dimensionless eccentricity, ϵ/h_0
ϵ = Eccentricity (µm)

Subscripts
0 = Concentric position
θ = Circumferential direction (rad)
a = Ambient
g = Groove
gr = Ratio groove to ridge
l = Land region
r = Ridge
t = Time-periodic
v = Particular NGT coefficient
x = x-direction in shaft cross-section plane
y = y-direction in shaft cross-section plane
z = Axial direction
c = Critical
per = Perturbed property

Acronyms
DFT = Discrete Fourier transformation
FEM = Finite element method
FGA = Finite groove approach
HGJB = Herringbone groove journal bearing
NGT = Narrow-groove theory
PDE = Partial differential equation

References
[1] Bonneau, D., Absi, J., 1994. Analysis of Aerodynamic Journal Bearings With Small Number of Herringbone Grooves by Finite Element Method. Journal of Tribology 116, 698–704. doi:10.1115/1.2927320.
[2] Bonneau, D., Huitric, J., Tournerie, B., 1993. Finite Element Analysis of Grooved Gas Thrust Bearings and Grooved Gas Face Seals. Journal of Tribology 115, 348–354. doi:10.1115/1.2921642.
[3] Castelli, V., Vohr, J., 1967. Performance characteristics of herringbone-grooved journal bearings operating at high eccentricity ratios and with misalignment. Mechanical technology Inc Latham NY .
[4] Constantinescu, V.N., Castelli, V., 2011. On the Local Compressibility Effect in Spiral-Groove Bearings. Journal of Lubrication Technology 91, 79–86. doi:10.1115/1.3554902.
[5] Cunningham, R.E., Fleming, D.P., Anderson, W.J., 1969. Experimental Stability Studies of the Herringbone-Grooved Gas-Lubricated Journal Bearing. Journal of Lubrication Technology doi:10.1115/1.3554896.
[6] Fleming, D.P., Hamrock, B.J., 1974. Optimization of self-acting herringbone journal bearing for maximum stability. NASA Technical Memorandum .
[7] Guenat, E., Schiffmann, J., 2018a. Effects of humid air on aerodynamic journal bearings. Tribology International 127, 333–340. doi:10.1016/j.triboint.2018.06.002.
[8] Guenat, E., Schiffmann, J., 2018b. Real-gas effects on aerodynamic bearings. Tribology International doi:10.1016/j.triboint.2018.01.008.
[9] Guenat, E., Schiffmann, J., 2019. Multi-Objective Optimization of Grooved Gas Journal Bearings for Robustness in Manufacturing Tolerances. Tribology Transactions 62, 1041–1050. doi:10.1080/10402004.2019.1642547.
[10] Hamrock, B., Fleming, D., 1971. Optimization of Self-Acting Herringbone Journal Bearings for Maximum Radial Load Capacity. NASA Technical Note .

[11] Hamrock, B.J., Schmid, S.R., Jacobson, B.O., 2004. Fundamentals of fluid film lubrication. CRC Press. doi:`10.1201/9780203021187`.

[12] Heinrich, J.C., Zienkiewicz, O.C., 1977. Quadratic finite element schemes for two-dimensional convective-transport problems. John Wiley & Sons Ltd. 11, 1831–1844. doi:`10.1002/nme.1620111207`.

[13] Hirs, G.G., 1965. The Load Capacity and Stability Characteristics of Hydrodynamic Grooved Journal Bearings. ASLE Transactions 8, 296–305. doi:`10.1080/05698196508972102`.

[14] Lund, J.W., 1968. Calculation of Stiffness and Damping Properties of Gas Bearings. Journal of Lubrication Technology 90, 793–803. doi:`10.1115/1.3601723`.

[15] Malanoski, S.B., 1965. Experiments on an ultra-stable gas journal bearing. Tribology 1, 62. doi:`10.1016/s0041-2678(68)80736-5`.

[16] Malanoski, S.B., Pan, C.H.T., 1965. The Static and Dynamic Characteristics of the Spiral-Grooved Thrust Bearing. Journal of Basic Engineering 87, 547–555. doi:`10.1115/1.3650603`.

[17] Miller, B.a., Green, I., 2001. Numerical Formulation for the Dynamic Analysis of Spiral-Grooved Gas Face Seals. Journal of Tribology 123, 395–403. doi:`10.1115/1.1308015`.

[18] Muijderman, E.A., 1965. Spiral Groove Bearings. Industrial Lubrication and Tribology 17, 12–17. doi:`10.1108/eb052769`.

[19] Rosset, K., Mounier, V., Guenat, E., Schiffmann, J., 2018. Multi-objective optimization of turbo-ORC systems for waste heat recovery on passenger car engines. Energy 159, 751–765. doi:`10.1016/j.energy.2018.06.193`.

[20] Salari, K., Knupp, P., 2000. Code Verification by the Method of Manufactured Solutions. Technical Report. Office of Scientific and Technical Information (OSTI). doi:`10.2172/759450`.

[21] Schiffmann, J., 2013. Enhanced Groove Geometry for Herringbone Grooved Journal Bearings. Journal of Engineering for Gas Turbines and Power 135, 102501. doi:`10.1115/1.4025035`.

[22] Schiffmann, J., 2015. Integrated Design and Multi-objective Optimization of a Single Stage Heat-Pump Turbocompressor. Journal of Turbomachinery 137, 071002. doi:`10.1115/1.4029123`.

[23] Vohr, J., Pan, C., 1964. On the spiral grooved, self-acting, gas bearing. Mechanical technology Inc Latham NY No. 63TR52.

[24] Vohr, J.H., Chow, C.Y., 1965. Characteristics of herringbone-grooved, gas-lubricated journal bearings. Journal of Basic Engineering 87, 568. doi:`10.1115/1.3650607`.

[25] Whipple, R., 1958. The inclined groove bearing. Technical Report. United Kingdom Atomic Energy Authority. Research Group. Atomic Energy Research Establishment. Harwell, Berks, England.

[26] Zhao, D., Blunier, B., Gao, F., Dou, M., Miraoui, A., 2014. Control of an ultrahigh-speed centrifugal compressor for the air management of fuel cell systems. IEEE Transactions on Industry Applications 50, 2225–2234. doi:`10.1109/TIA.2013.2282838`.

Appendix A: Grid sensitivity study
Appendix B: Solver computation time comparison
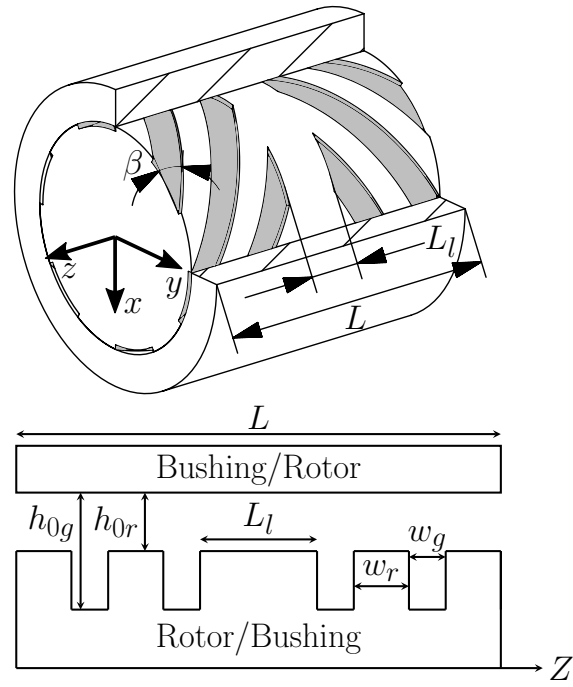
List of Figures

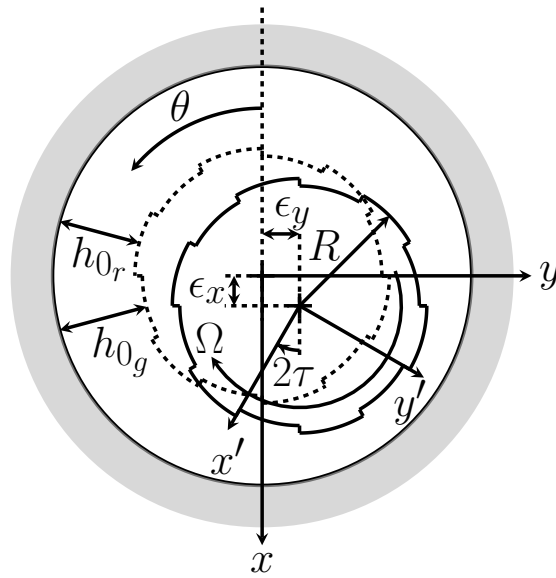Fig. 1: Herringbone grooved journal. Bearing design parameters.

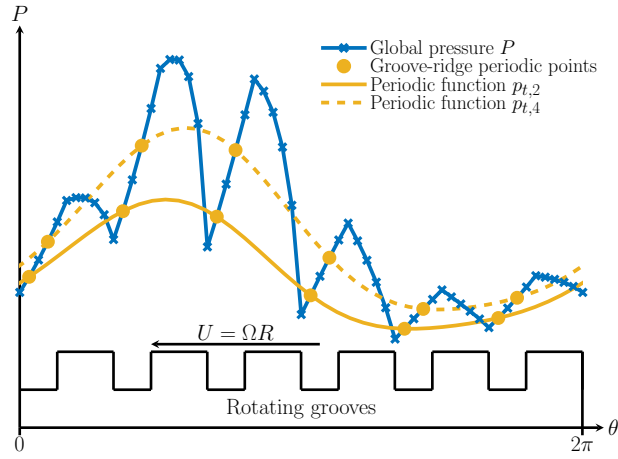Fig. 2: Bearing convention for grooves attached to rotating journal.

Fig. 3: Evolution of pressure measured within the rotating frame at two angular positions ($\theta_1 = 2\pi/(10 N_g)$ and $\theta_4 = 6\pi/(10 N_g)$ with $10 N_g$ mesh points in the circumferential direction) within a groove-ridge pair (yellow), compared to the pressure measured in the stationary reference frame at time $\tau = 0$ (blue) for a grooved rotor at a constant static eccentricity.
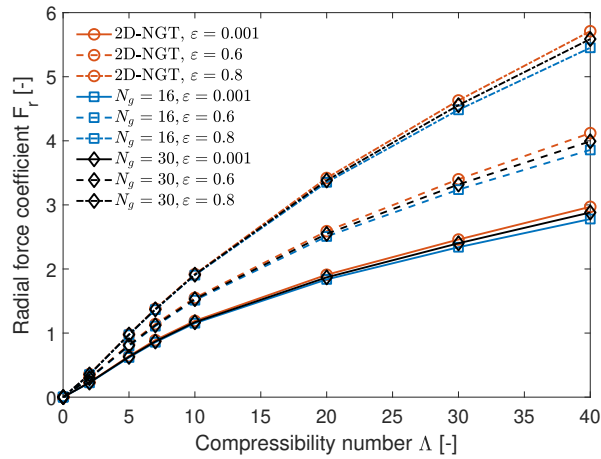
Fig. 4: Radial force coefficient versus compressibility number for non-rotating grooves. Comparison of 2D-NGT solution and FEM solution with different number of grooves. 2D-NGT: infinite number of grooves, $N_g = 16$: 16 grooves, $N_g = 30$: 30 grooves. Eccentricities $\varepsilon = 0.001, 0.6, 0.8$.
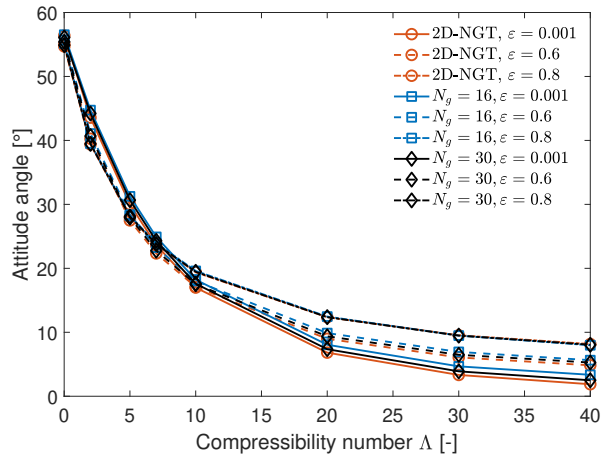
Fig. 5: Attitude angle versus compressibility number for non-rotating grooves. Comparison of 2D-NGT solution and FEM solution with different number of grooves. 2D-NGT: infinite number of grooves, $N_g = 16$: 16 grooves, $N_g = 30$: 30 grooves. Eccentricities $\varepsilon = 0.001, 0.6, 0.8$.
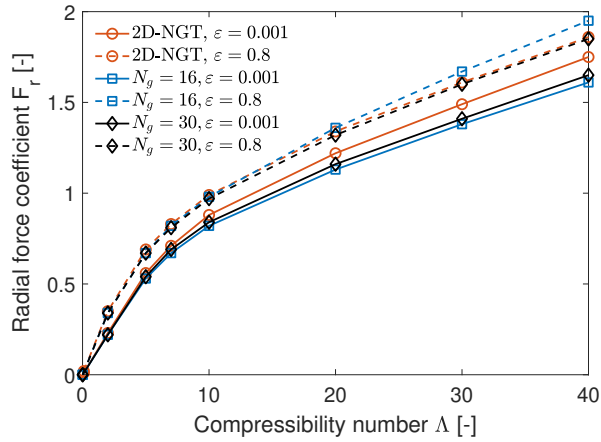
Fig. 6: Radial force coefficient versus compressibility number for rotating grooves. Comparison of 2D-NGT solution and FEM solution with different number of grooves. 2D-NGT: infinite number of grooves, $N_g = 16$: 16 grooves, $N_g = 30$: 30 grooves. Eccentricities $\varepsilon = 0.001, 0.8$.
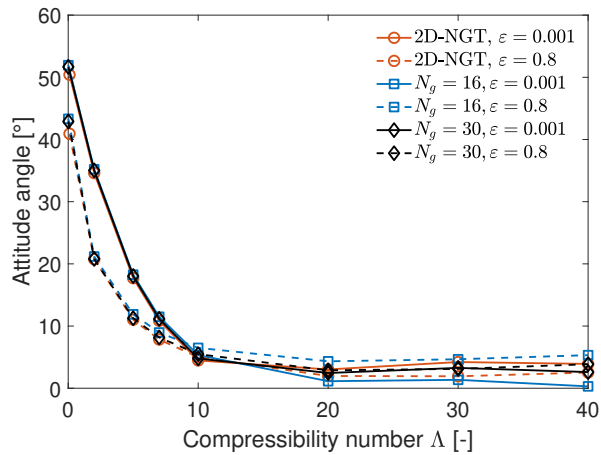
Fig. 7: Attitude angle versus compressibility number for rotating grooves. Comparison of 2D-NGT solution and FEM solution with different number of grooves. 2D-NGT: infinite number of grooves, $N_g = 16$: 16 grooves, $N_g = 30$: 30 grooves. Eccentricities $\varepsilon = 0.001, 0.8$.

(a) ε = 0.01

(b) ε = 0.4

(c) ε = 0.6

(d) ε = 0.8
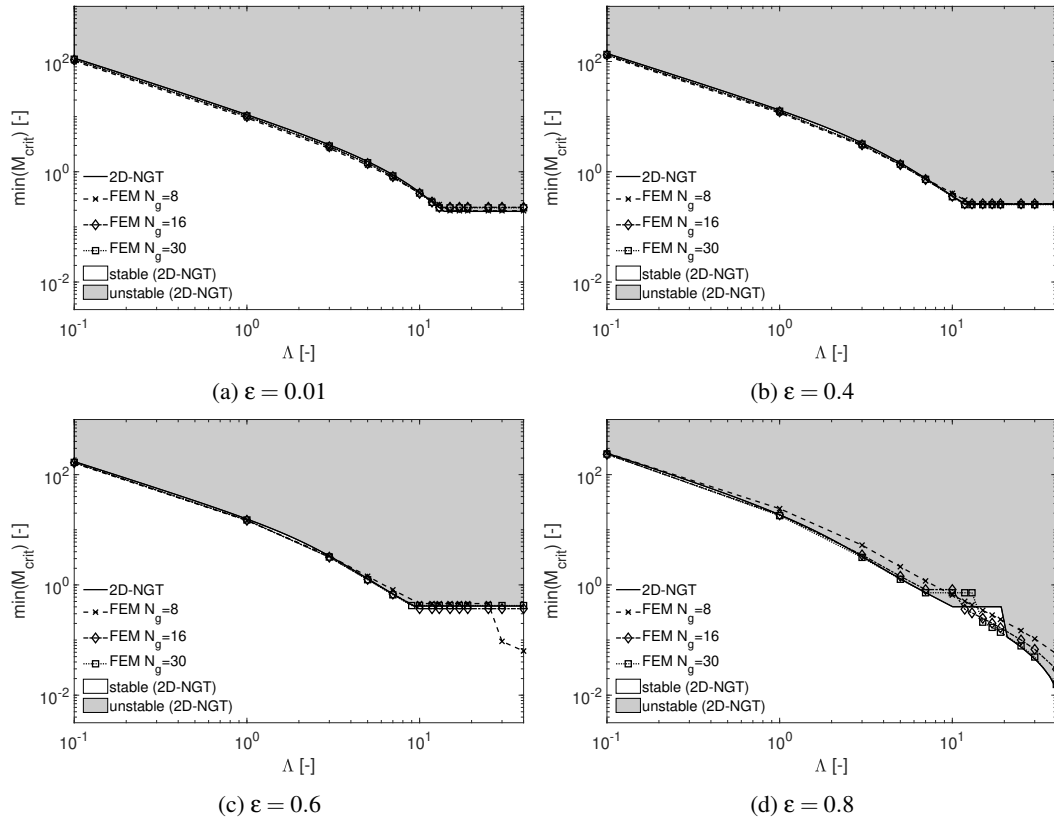
Fig. 8: Stability maps of bearing with stationary grooves at different eccentricities.

(a) ε = 0.01

(b) ε = 0.4

(c) ε = 0.6

(d) ε = 0.8
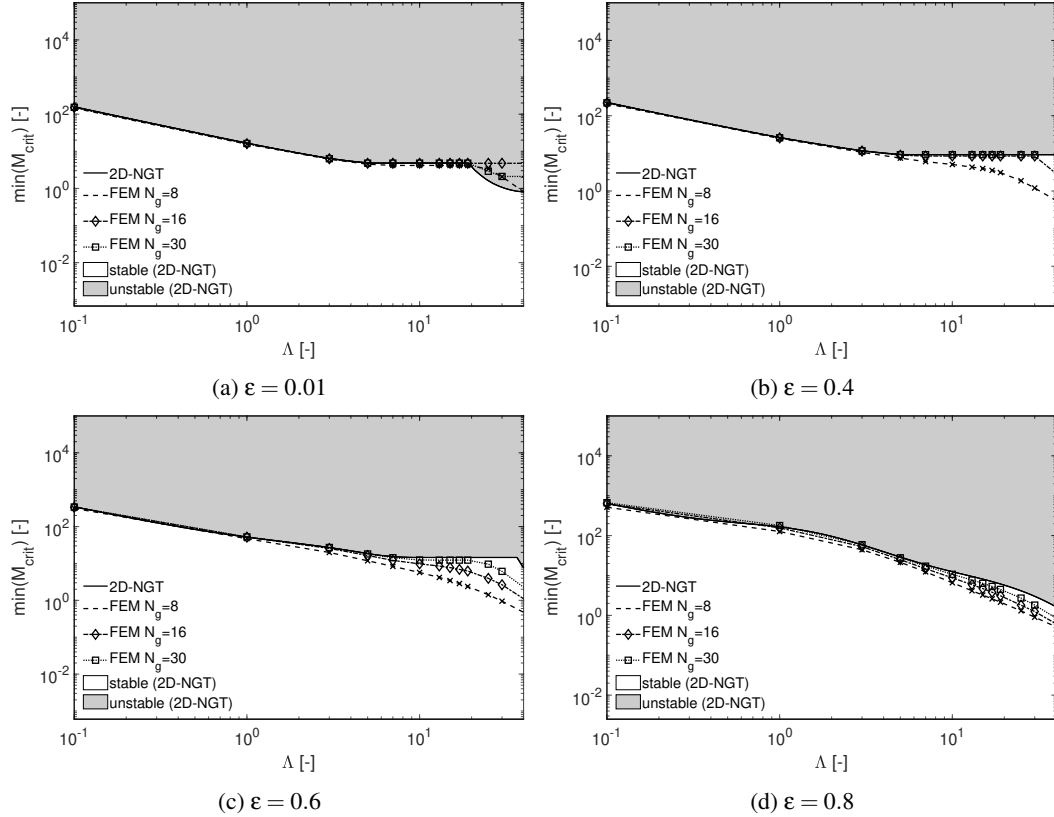
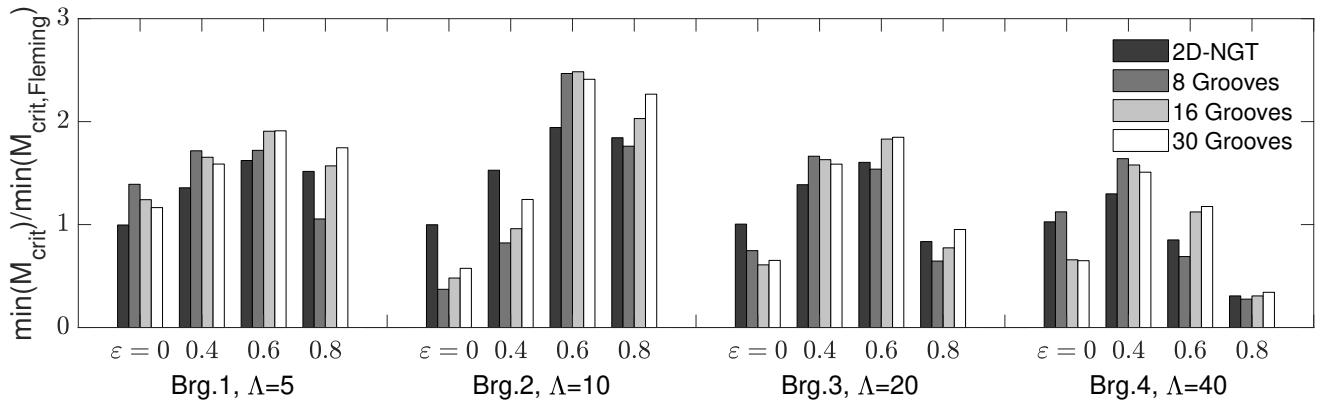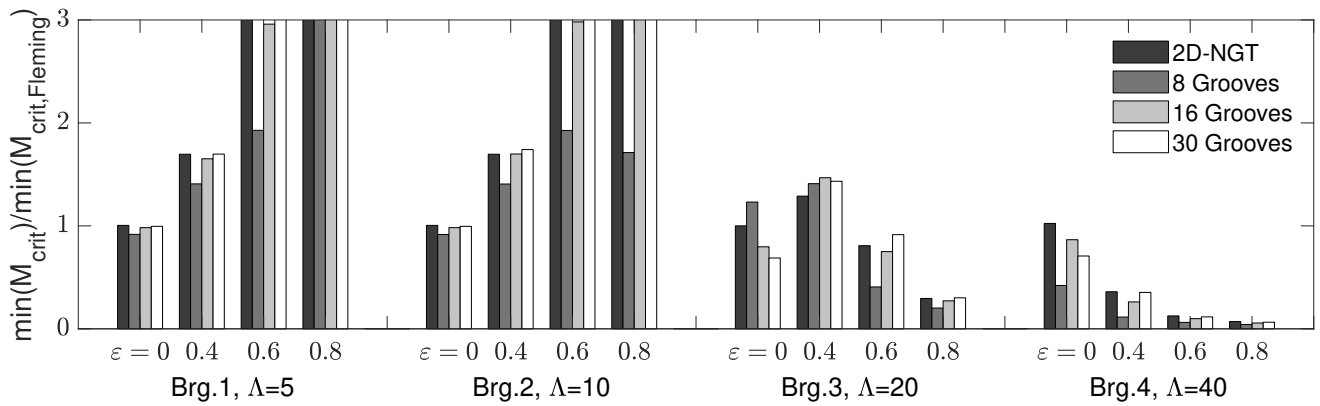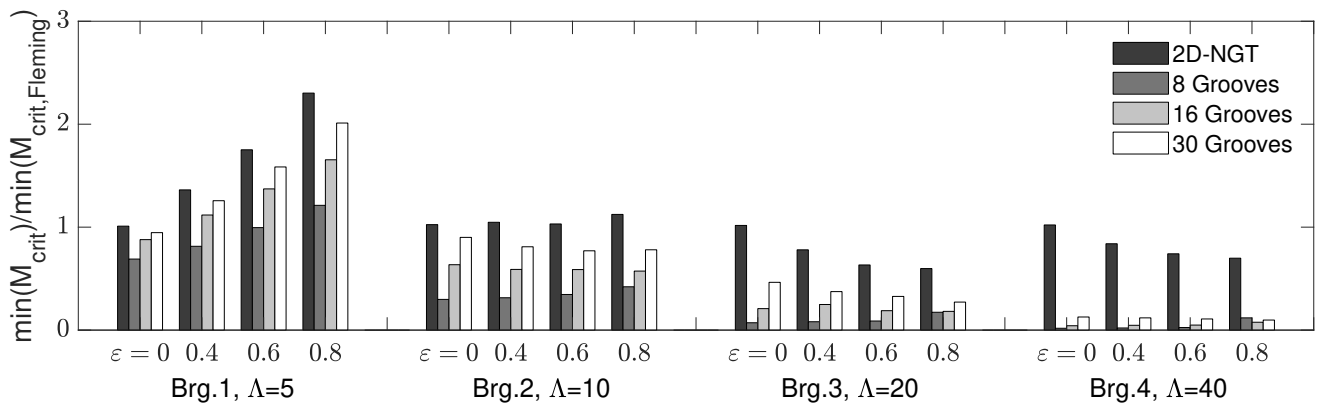Fig. 9: Stability maps of bearing with rotating grooves at different eccentricities.

Fig. 10: Rotating grooves with $L/D = 0.5$. Comparison of minimum critical mass at different eccentricities with optimized bearings by Fleming et al. [6]. Bearings with 16 and 30 grooves are solved by the time-periodic computation method.


Fig. 11: Rotating grooves with $L/D = 1$. Comparison of minimum critical mass at different eccentricities with optimized bearings by Fleming et al. [6]. Bearings with 8, 16 and 30 grooves are solved by the time-periodic computation method.

Fig. 12: Rotating grooves with $L/D = 2$. Comparison of minimum critical mass at different eccentricities with optimized bearings by Fleming et al. [6]. Bearings with 16 and 30 grooves are solved by the time-periodic computation method.
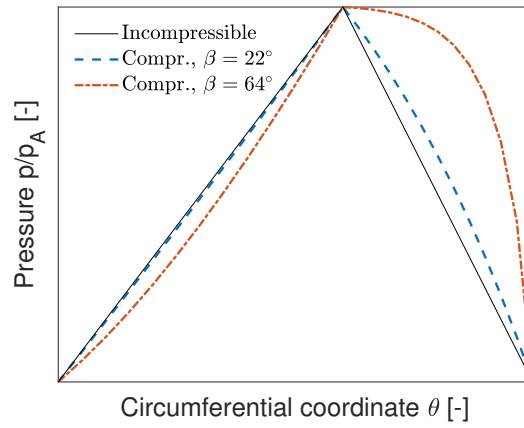
Fig. 13: Compressible pressure profile over rotating groove-ridge pair at 25 % of axial bearing length. Different groove angles β, compared with incompressible pressure distribution. Bearing load and geometry: $\varepsilon = 0, \Lambda = 40, L/D = 2, \alpha = 0.6, \gamma = 1$ and $H_{gr} = 2.68$.
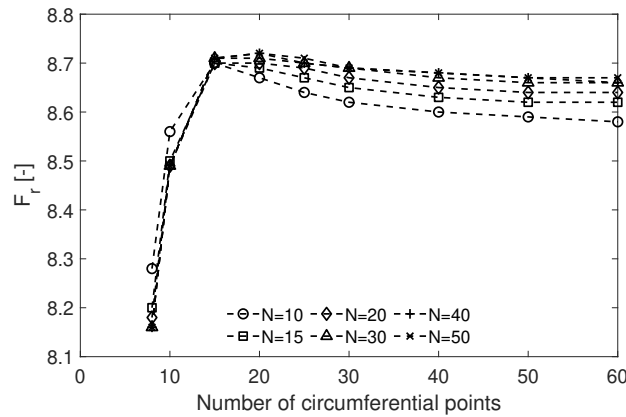

Fig. 14: Grid sensitivity analysis for 2D-NGT-solver with non-rotating grooves. Radial force coefficient vs. number of circumferential mesh points. N: number of mesh points in axial direction for symmetric bearing. ($\Lambda = 70, \varepsilon = 0.8$)
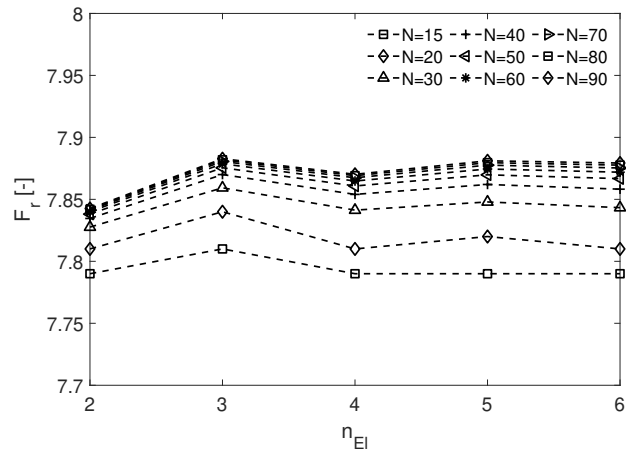

Fig. 15: Grid sensitivity analysis for FEM bi-linear solver with non-rotating grooves. Radial force coefficient vs. number of elements per each groove and each ridge. N: number of mesh points in axial direction for symmetric bearing. ($\Lambda = 70, \varepsilon = 0.8$)
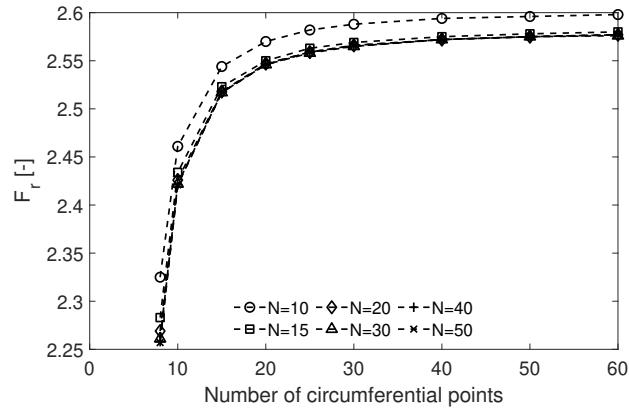
Fig. 16: Grid sensitivity analysis for 2D-NGT-solver with rotating grooves. Radial force coefficient vs. number of circumferential mesh points. N: number of mesh points in axial direction for symmetric bearing. ($\Lambda = 70$, $\varepsilon = 0.8$)
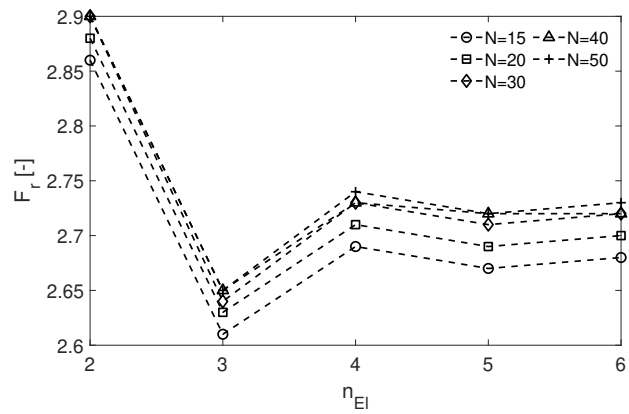

Fig. 17: Grid sensitivity analysis for FEM bi-linear solver with 16 rotating grooves. Radial force coefficient vs. number of elements per each groove and each ridge. N: number of mesh points in axial direction for symmetric bearing. ($\Lambda = 70$, $\varepsilon = 0.8$)

List of Tables

Table 1: Herringbone-grooved journal bearing parameters

Parameter	Symbol and Expression	Unit
Diameter	D	m
Length to diameter ratio	L/D	-
Groove angle	β	°
Groove width ratio	$\alpha = w_g/(w_g + w_r)$	-
Groove length ratio	$\gamma = (L - L_l)/L$	-
Film thickness ratio	$H_{gr} = h_{0g}/h_{0r}$	-
Number of grooves	N_g	-

Table 2: Used mesh sizes for the different solvers. N: number of mesh points in axial direction for one half of the bearing (symmetric bearing). N_θ: number of points in circumferential direction. n_{El}: number of points per each groove and each ridge.

Solver	N	
2D-NGT non-rotating grooves	50	$N_\theta = 80$
2D-NGT rotating grooves	20	$N_\theta = 50$
FEM bi-linear non-rotating grooves	70	$n_{El} = 3$
FEM bi-linear rotating grooves	30	$n_{El} = 4$

Table 3: Comparison of CPU time of FGA, NGT and transient time integration method for rotating grooves. CPU specification: Intel(R) Core(TM) i7-8550U at 1.8GHz.

Solver	Elements	CPU time (s)
Transient	2784	2223
FGA	2784	20
NGT	1911	0.57